

TECHNICAL REPORT #37

Smithsonian Institution &
The University of Arizona*

**An Interferometric Hartmann Wavefront Analyzer
for the 6.5m MMT, and the First Results for
Collimation and Figure Correction**

S. C. West, S. Callahan, D. Fisher

June 2001

An Interferometric Hartmann Wavefront Analyzer for the 6.5m MMT, and the First Results for Collimation and Figure Correction

S. C. West (swest@as.arizona.edu), S. Callahan, and D. Fisher¹
Multiple Mirror Telescope Observatory

MMTO Technical Report #37, June 2001
http://nemo.as.arizona.edu/~swest/pdfs/ih_sh.pdf (color version)

Abstract

The theory, optical, mechanical, and software design for an interferometric Hartmann wavefront analyzer for the 6.5 m MMT is presented. The instrument is modular so it can be used at the prime focus or any of the three unique Cassegrain foci. We discuss the first results at the f/9 Cass focus where the detected wavefront error was used to correct both collimation and the primary mirror figure distortion. Despite the fact that neither M1 nor M2 were thermally controlled at the time, it is found that two correction iterations produce an image psf near 0.1 arcsec p-p.

I. Overview

The 6.5m MMT will have 3 Cassegrain foci -- f/9, f/5, and f/15. The MMTO will provide facility wavefront sensors for the f/9 and f/5 focal modes. The f/15 instrumentation will have dedicated wavefront sensing provided by Steward Observatory's CAAO group tailored for the use of adaptive secondary mirrors.

The facility wavefront analyzers consist of two types. The first is a relatively high resolution modular wavefront analyzer whose configuration can be changed for use at either the prime, f/9, f/5 or f/15 foci. This provides over 30 phase apertures across the pupil diameter. It is primarily intended for stand-alone opto-mechanical studies of the optics, mirror support systems, telescope support structure, and the construction of elevation and temperature-dependent look-up tables. The instrument is based on the interferometric Hartmann (or Korhonen-Hartmann) technique invented at the Nordic Optical Telescope (NOT) and also used at the Vatican Advanced Technology Telescope (VATT) [1-6]. The second type of wavefront sensor resides permanently at the f/9 and f/5 Cassegrain foci. They have not yet been constructed, but will most likely be Shack Hartmann or curvature sensing units. They will provide nightly routine refinements to the look-up table collimation and figure correction.

Section II presents a brief overview of the theory of the interferometric Hartmann technique and contrasts it to a Shack Hartmann device. Section III outlines the design and opto-mechanics of the interferometric Hartmann analyzer. Section IV explains how the wavefront error is determined from the phase-differences detected by the analyzer. Section V summa-

rizes the first results of active figure correction and collimation at the f/9 focus of the 6.5m MMT. Section VI explains our development of interactive software for collecting and analyzing wavefront data.

II. The Interferometric Hartmann Technique

The interferometric Hartmann analyzer directly measures wavefront phase differences in contrast to the Shack-Hartmann which measures wavefront gradients. Instead of a lenslet array, the interferometric device uses a simple Hartmann aperture mask array placed at the collimated re-imaged pupil. A single converging lens focuses the Airy patterns produced by the apertures. The relatively large Airy patterns overlap each other in the extra and intra focal areas adjacent to the focus. Groups of 4 adjacent apertures (a quartet) produce sharp interference in these overlapping regions. The position of the interference spots depends upon the phase differences in the corresponding 4 apertures.

The size of the diffraction spot from the Shack Hartmann lenslet is inversely proportional to the diameter of the lenslet ($2.44/D$), while the size of the interference spot from the Korhonen device is inversely proportional to the separation between apertures ($1/d$). Therefore, the interference spot can be made up to 7 times smaller than the corresponding spot from a Shack Hartmann device. Insofar as the accuracy of the centroiding algorithm increases with decreasing spot size, the accuracy in detected wavefront errors increases.

The position of the $m=0$ diffraction spot depends upon the phase differences between the 4 apertures. It is sensitive to all sources of phase difference (*including piston*, to which the

1. Now at the University of Arizona Center for Astronomical Adaptive Optics.

Shack Hartmann is insensitive). The unwanted $m=\pm 1$ diffraction is controlled by adjusting the aperture diameter (to modulate the $m = \pm 1$ intensities) and the aperture separation (to adjust the angular separation of the $m=0$ and $m = \pm 1$ diffraction peaks) as illustrated in Figure 1.

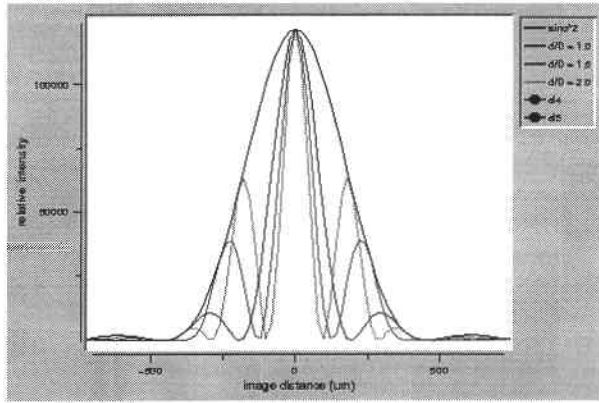


Figure 1: One dimensional diffraction formed by two Hartmann apertures (with identical phases) for several ratios of aperture-spacing to diameter (1, 1.5, and 2). This illustrates how the geometry is used to control suppression of unwanted interference orders. The intensity of the interference fringes is modulated by the diffraction envelope of a single aperture. The ratio of $d/D=1$ has the advantage of offering the best high-order suppression but has the disadvantages of having the widest $m=0$ fringe and more spatial averaging of the pupil phase function for a given spacing.

A significant limitation to the interferometric Hartmann technique is dynamic range. As the phase difference increases, the $m=0$ fringe shifts away from the center of the aperture diffraction. At the same time, one of the $m = \pm 1$ fringes shifts towards the center of the aperture diffraction. Soon the spot centroiding routine becomes confused. Therefore this technique is best employed when the optics are already well on their way to being optimized. In practice, we have found this technique capable of measuring wavefronts with as much as a micron or two of wavefront aberration in several modes. Korhonen at the NOT reports being able to measure up to 10 microns of wavefront coma (private communication). Employing a finer Hartmann mask gives the device higher dynamic range because the phase difference is smaller between apertures.

Enlarging the optical bandpass has several advantages: 1) the instrument collects more light, 2) the $m=0$ interference fringes for different wavelengths overlap, and 3) the higher order fringes smear out into spectra helping to reduce their unwanted effects as shown in Figure 2.

For ease of illustration, the figures have been shown with the detector at the focus of the lens. However at this position, adding more Hartmann apertures simply causes the interference

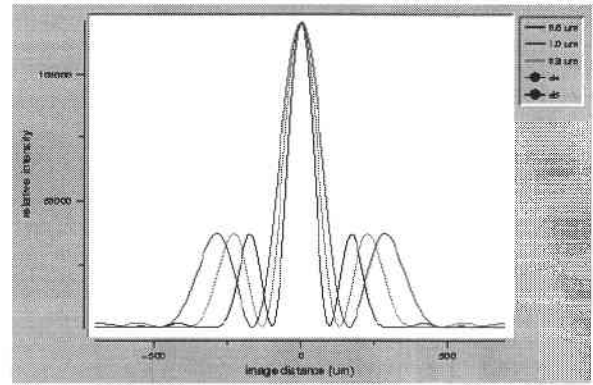


Figure 2: Interference shown for 3 wavelengths in a bandpass (0.6 blue, 0.8 green, and 1.0 micron). The $m=0$ fringes overlap while the higher orders “smear” into spectra reducing their unwanted effects.

fringes to become sharper, just like adding more rulings to a diffraction grating.

In order to detect the phase difference distribution throughout the entire pupil, the detector is placed either inside or outside of the lens focus so that adjacent $m=0$ diffraction peaks are spatially separated on the detector. The shift of the detector away from the lens focus is constrained by two criteria. The first is that the defocused airy patterns produced by the Hartmann apertures must significantly overlap to produce interference. The second constraint is to achieve the desired spacing between successive $m=0$ interference fringes. Typically, one places a given $m=0$ interference fringe onto the $m=\pm 1$ fringe of the adjacent pattern or onto the minimum of the adjacent de-focussed sinc^2 aperture function.

Figure 3 shows diffraction created by a line of 8 Hartmann

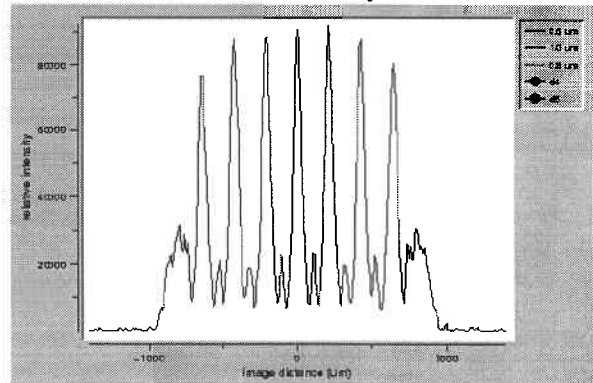


Figure 3: One dimensional diffraction formed with a line of 8 Hartmann apertures (with equal phases). The detector is shifted away from the lens focus to separate the $m=0$ fringes.

apertures when the detector is shifted away from the focus of the lens. Each pair of apertures produces a distinct $m=0$ interference. The edges of the pattern show residual higher order diffraction.

The diffraction effect of a 1/8-wave phase shift in one aperture is shown in Figure 4. Here, 5 apertures are modelled with a

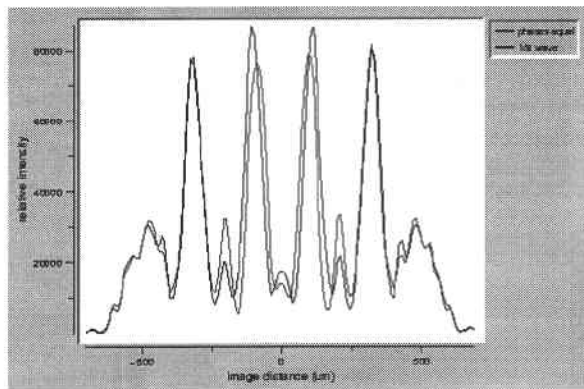


Figure 4: One-dimensional model of diffraction created by 5 Hartmann apertures in a line: with all phases equal (black) and with the center aperture having a phase shift of +1/8-wave. The two central fringes are shifted inward by the phase error. This is how phase differences are detected using an interferometric Hartmann wavefront analyzer. In practice though, the interference pattern is in two dimensions and each interference maximum is created by 4 apertures.

phase shift of +1/8 wave of piston in the center aperture. The two center $m=0$ fringes have shifted towards one another. This is how the interferometric Hartmann technique works except that in practice, the $m=0$ interference is formed in 2 dimensions by 4 apertures as described in section IV. The direction and magnitude of the spot shifts is proportional to the phase differences in the apertures.

III. Instrument Design

This section describes the opto-mechanical design of the interferometric Hartmann for the 6.5m MMT.

A. f/9 module

Two Apogee KX-260 CCD cameras were selected for use with the instrument (512 x 512 with 20 micron pixels). The optical design (using OSLO PRO) was driven to match the interferogram to this detector format. The Cassegrain f/9 module of the instrument is shown in Figure 5. The optics are very simple. A doublet collimator (MG 06 LAI 015) forms a pupil image. A Hartmann mask and blue-cutoff filter (RG 715) are placed at the pupil. Immediately following the pupil is a doublet focussing lens (MG 06 LAI 015). The interferogram is formed between this lens and its focus. A focal plane turret allows the user to select between a tilted pierced acquisition mirror or a laser diode reference source. The acquisition channel incorporates a 1:1 re-imager so the focal scale of the telescope is preserved. The geometry of the Hartmann mask is also shown in Figure 5. The ratio of aperture spacing to diameter was chosen to be 1.5.

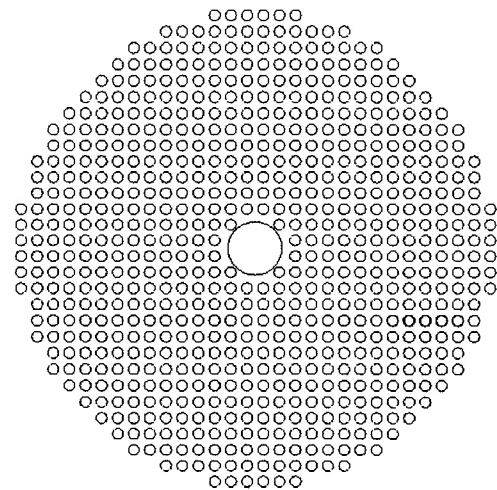
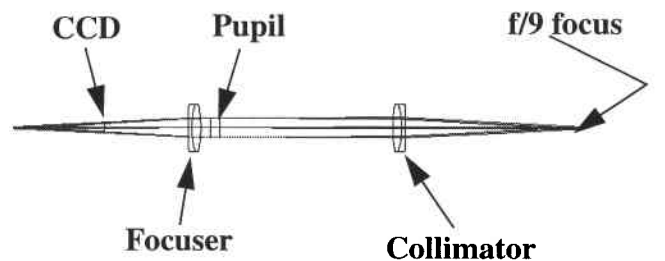
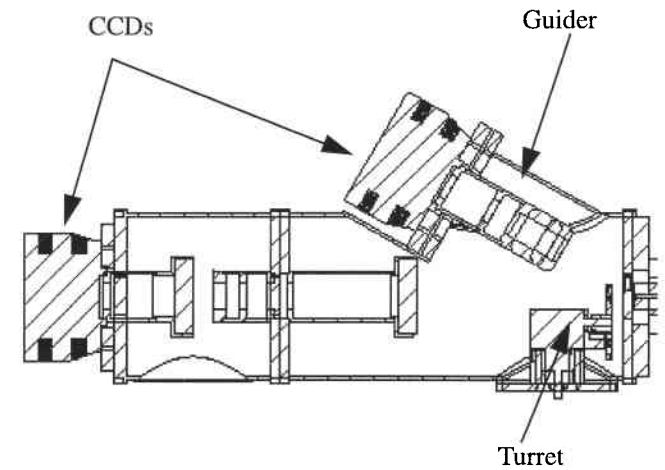


Figure 5: The Cassegrain f/9 module of the interferometric Hartmann wavefront sensor. A collimator forms a pupil where the Hartmann mask and filter are placed. A focussing lens is placed behind the Hartmann mask. The interferogram is formed between this focus and the lens. The turret provides a tilted pierced mirror for guiding and acquisition or a laser diode reference. The lower figure shows the geometry of the Hartmann mask in the 30mm diameter pupil.

The section of the instrument containing the Hartmann mask and focussing lens is replaceable to allow reconfiguration for the other Cassegrain foci of the telescope.

B. prime focus module

An $f/1.25$ to $f/9$ beam converter module was built to allow wavefront analysis at the prime focus of the telescope. The intention is to allow the primary mirror to be studied and characterized independent of the secondary mirror. This module is shown in Figure 6. The diode laser collimator creates a inter-

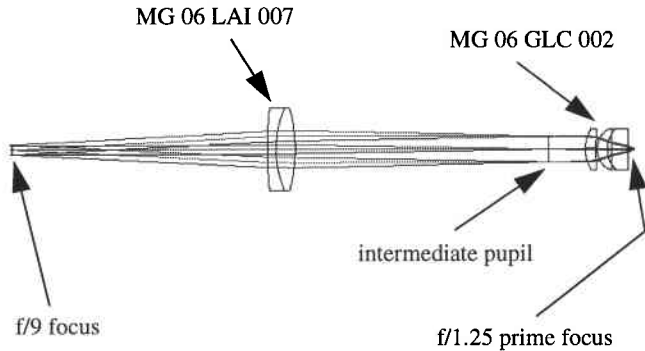


Figure 6: The prime focus beam converter attaches to the forend of the $f/9$ module. It uses a diode laser collimator (GLC 002) and an auxiliary lens (LAI 007) to convert the $f/1.25$ prime focus beam to $f/9$ for input into the $f/9$ module shown in Figure 7. In addition to changing the beam speed, the LAI 007 reimages the pupil formed by the diode collimator back to infinity for compatibility with the $f/9$ module..

mediate pupil that is re-imaged back to infinity by the auxiliary doublet. The final beam is compatible with the $f/9$ module of the instrument.

A removable $f/1.0$ reference source was constructed using a diode laser and microscope objective so that the aberrations of the instrument optics could be removed from the observed wavefront aberrations at the telescope. However, the final wavefront errors include errors produced by the microscope objective reference, but as Figure 8 implies, these are very small.

This module was intended to be used in the period prior to the telescope dedication (May 2000) before the secondary system was installed. Unfortunately, this period was too brief to obtain the observations. Perhaps it will be used in the future. The prime focus module includes a cone connection to the mobile plate of the hexapod, so the instrument can be precisely positioned. The entire prime focus configuration is shown in Figure 7.

C. instrument aberrations

As noted above, each module contains a reference source to allow the removal of the instrument aberrations from the observed wavefront errors. Figure 8 shows interferograms created with the laser diode reference sources for the $f/9$ and $f/1$

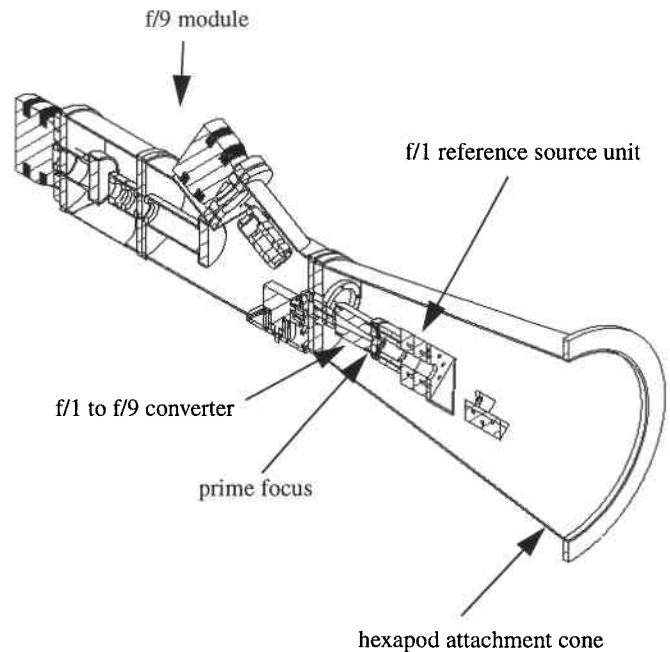


Figure 7: A cut-away view of the prime focus module attached to $f/9$ unit.

prime focus modules. Both show very little aberration and low geometric distortion. Higher order $m=\pm 1$ diffraction can be seen around the periphery and center of the spot pattern. The bright feature at the center is created by a large hole in Hartmann mask.

IV. Determining the Wavefront Error

Whether a Shack or interferometric Hartmann analyzer is used, the same basic data reduction is required. One must subtract the instrumental wavefront errors from the wavefront errors sampled in a re-imaged telescope pupil. The resulting wavefront error distribution is fitted to a set of polynomials (or used to reconstruct raw phases) which are then used to describe the telescope collimation errors and required active bending of the primary mirror. The Shack Hartmann device measures the x and y wavefront gradients at the sampling points within the pupil, and the interferometric Hartmann device measures the x and y phase differences produced by quartets of Hartmann apertures.

A. Gradient solution

We start with M sampling points within the pupil. For each point i , centered on the dimensionless pupil coordinate (x_i, y_i) , we determine the total x and y wavefront gradients $((\partial W_i)/\partial x, (\partial W_i)/\partial y)$. The gradient information is obtained by directly with a Shack Hartmann, but must be computed from phase differences with the interferometric device.

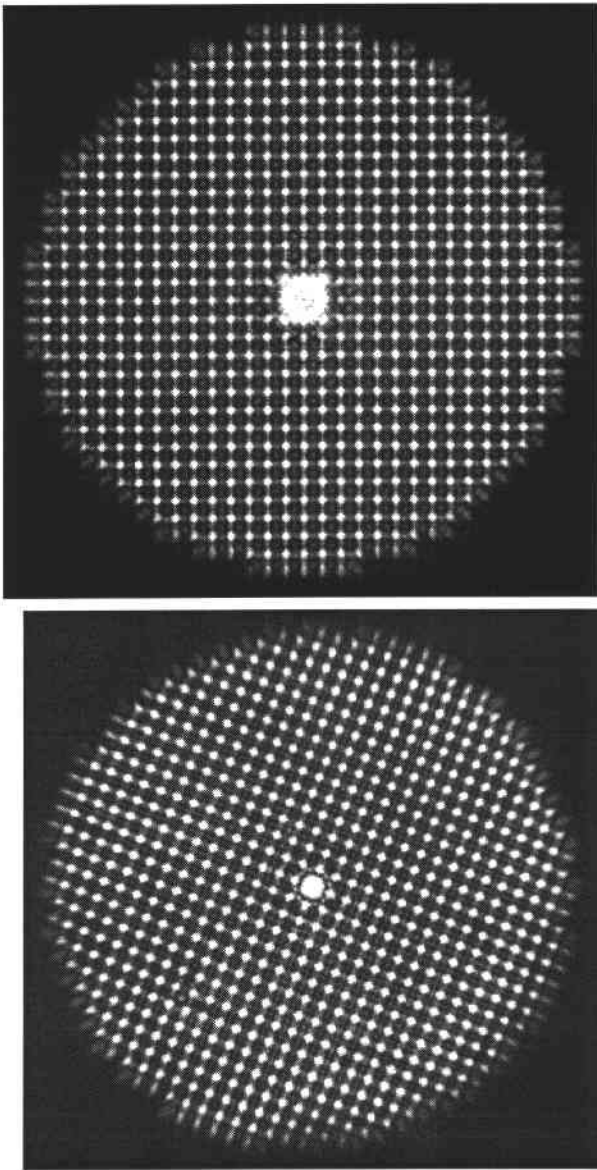


Figure 8: System interferograms created with a laser diode reference source for the $f/9$ (top) and the $f/1$ prime focus configurations.

The wavefront at a given point W_i is described by N polynomials Z_j with coefficients C_j by:

$$W(x_i, y_i) = \sum_{j=1}^N (Z_j(x_i, y_i)C_j) = W_i \quad (1)$$

Appendix A provides a description of the wavefront polynomials, their gradients, and pictures of the pupil phase distributions and corresponding image psfs.

The matrix equation describing the relationship of the wavefront error gradients to the polynomial gradients is then

$$\begin{bmatrix} \frac{\partial Z_1}{\partial x} \Big|_{x_1, y_1} & \dots & \frac{\partial Z_N}{\partial x} \Big|_{x_1, y_1} \\ \dots & \dots & \dots \\ \frac{\partial Z_1}{\partial x} \Big|_{x_M, y_M} & \dots & \frac{\partial Z_N}{\partial x} \Big|_{x_M, y_M} \\ \frac{\partial Z_1}{\partial y} \Big|_{x_1, y_1} & \dots & \frac{\partial Z_N}{\partial y} \Big|_{x_1, y_1} \\ \dots & \dots & \dots \\ \frac{\partial Z_1}{\partial y} \Big|_{x_M, y_M} & \dots & \frac{\partial Z_N}{\partial y} \Big|_{x_M, y_M} \end{bmatrix} \begin{bmatrix} C_1 \\ \dots \\ C_N \end{bmatrix} = \begin{bmatrix} \frac{\partial W_1}{\partial x} \\ \dots \\ \frac{\partial W_M}{\partial x} \\ \frac{\partial W_1}{\partial y} \\ \dots \\ \frac{\partial W_M}{\partial y} \end{bmatrix} \quad (2)$$

Each column describes the influence one polynomial has on the wavefront gradient. This has the form of $[A](x) = (b)$, where $[A]$ is a $2M \times N$ matrix. We solve for the polynomial coefficients (x) using singular value decomposition (SVD).

Eq. 2 can be used with the interferometric instrument since the phase differences can be converted to gradients. The wavefront is smoothed and the resolution decreased since there is only one gradient computed per aperture quartet.

B. Phase reconstruction

An interference spot formed by an aperture quartet is shown in Figure 9. The view is along the optic axis. The 4 apertures are

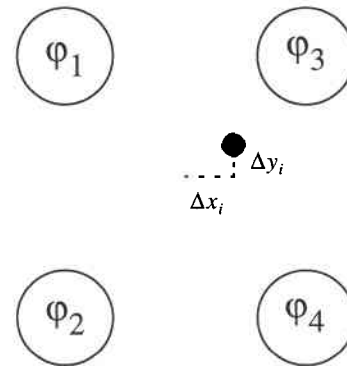


Figure 9: Looking down the optic axis, the i th $m=0$ interference (dark spot) is shown between the 4 pupil apertures that create it. The spot is exactly centered between the apertures only if the individual phases are equal. Unequal phases cause a shift in the spot position proportional to the phase differences in the apertures.

in the pupil plane while the interference spot is formed on the CCD by a converging lens placed near the lens focus.

The position of the interference spot depends on the individual phases in the four apertures:

$$\Delta\phi_{x_i} = [(\phi_1 + \phi_2) - (\phi_3 + \phi_4)] = (\Delta x_i) \left(\frac{\text{nm phase shift}}{\text{pixel}} \right) \quad (3)$$

$$\Delta\phi_{y_i} = [(\phi_2 + \phi_4) - (\phi_1 + \phi_3)] = (\Delta y_i) \left(\frac{\text{nm phase shift}}{\text{pixel}} \right) \quad (4)$$

where Δx_i , Δy_i are measured directly on the detector. The constant of proportionality is the distance from the $m=0$ to $m=1$ fringe scaled onto the detector.

Neglecting piston, the spot displacements can be converted into wavefront gradients by:

$$\frac{\partial W_i}{\partial x} = \frac{\Delta\phi_{x_i}}{2\text{ap_sp}} \quad (5)$$

$$\frac{\partial W_i}{\partial y} = \frac{\Delta\phi_{y_i}}{2\text{ap_sp}} \quad (6)$$

where ap_sp is the Hartmann aperture spacing projected onto the dimensionless pupil.

A mode-independent phase reconstruction may be found using a method similar to the matrix formulation of Hunt 1979 [7]. Again we have M total samplings of the phases differences within the pupil, and we have (K) phase apertures. The individual phases are solved with the following matrix equation. Since $M \sim K \gg N$, the major disadvantage of this solution is the longer time required to invert the matrix compared to Eq 2.

$$\begin{bmatrix} 1 & 1 & -1 & -1 & 0 & \dots & \dots & 0 \\ 0 & 0 & 1 & 1 & -1 & -1 & 0 & \dots & \dots & 0 \\ \dots & \dots & \dots & \dots & \dots & \dots & \dots & \dots & \dots & \dots \\ 0 & \dots & \dots & 0 & 1 & 1 & -1 & -1 & \dots & \dots \\ -1 & 1 & -1 & 1 & 0 & \dots & \dots & \dots & \dots & 0 \\ 0 & 0 & -1 & 1 & -1 & 1 & 0 & \dots & \dots & 0 \\ \dots & \dots & \dots & \dots & \dots & \dots & \dots & \dots & \dots & \dots \\ 0 & \dots & \dots & 0 & -1 & 1 & -1 & 1 & \dots & \dots \end{bmatrix} \begin{bmatrix} \phi_1 \\ \dots \\ \phi_K \end{bmatrix} = \begin{bmatrix} \Delta\phi_{x_1} \\ \dots \\ \Delta\phi_{x_M} \\ \Delta\phi_{y_1} \\ \dots \\ \Delta\phi_{y_M} \end{bmatrix} \quad (7)$$

Once the phases are found, they can be fit to wavefront polynomials with another application of SVD:

$$\begin{bmatrix} Z_1(x_1, y_1) & \dots & \dots & Z_N(x_1, y_1) \\ \dots & \dots & \dots & \dots \\ Z_1(x_K, y_K) & \dots & \dots & Z_N(x_K, y_K) \end{bmatrix} \begin{bmatrix} C_1 \\ \dots \\ C_N \end{bmatrix} = \begin{bmatrix} \phi_1 \\ \dots \\ \phi_K \end{bmatrix} \quad (8)$$

C. Calculation of primary mirror force distribution

Once the phase error distribution of the pupil is determined, coma and focus are used to adjust the secondary position, and the other coefficients are used to compute the axial force dis-

tribution that corrects primary mirror distortion. The details of that calculation are beyond the scope of this memo, but can be found elsewhere [8,9].

V. First Results

During the period spanning August through October 2000, the instrument was periodically attached to the 6.5m telescope (Figure 10). Unusually inclement weather limited useful

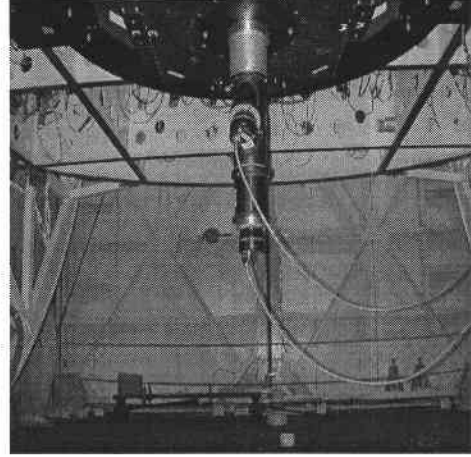


Figure 10: The interferometric Hartmann wavefront sensor attached to the $f/9$ top box of the 6.5m MMT. Using the instrument rotator, the Hartmann apertures of the wavefront analyser were carefully aligned with the axes of the primary mirror support system.

observations to just over 4 partial nights. The program was meant to test the effectiveness of the interferometric instrument to reliably measure the wavefront errors and the ability of those errors to be used to correct mirror figure and collimation.

A typical stellar interferogram is show in Figure 11. At this very early stage of the telescope's life, the integration time was long enough (30 sec.) to average out most of the effects of seeing but short enough to accommodate errors in tracking. Interestingly, the M2 support vanes do not appear to significantly affect phase detection when oriented 45-deg to the pattern rows and columns.

Wavefront aberrations were calculated after averaging 3-5 of these 30-sec. exposures which typically produced wavefront coefficients that repeated with sub-10 nm p-p variation.

Figure 12 shows a typical set of observed starting aberrations (red bars) for 14 Zernike modes excluding solid-body piston

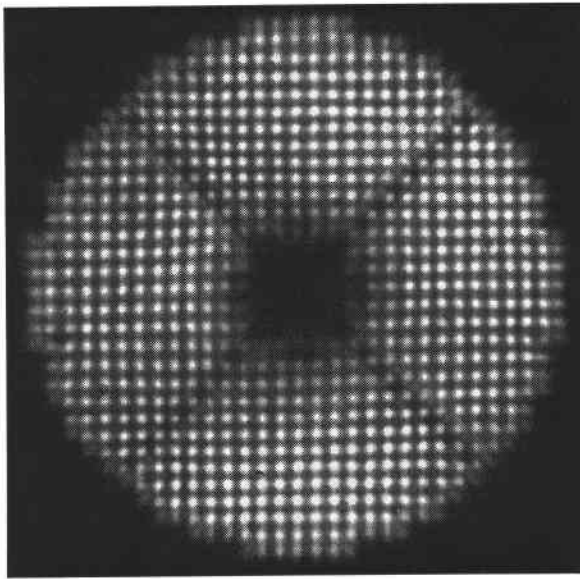


Figure 11: Typical interferogram of a stellar wavefront at the $f/9$ focus of the MMT for an integration of 30 sec. There was no thermal control of either the primary or secondary borosilicate mirrors.

and the two global tilts. The modes are defined in Table 1. It's

Table 1: Mode definitions for Figure 12.

Mode #(s)	Description
1	defocus
2-3	astigmatism
4-5	coma
6	spherical
7-8	trefoil
9-10	5th order astig
11-12	quatrefoil
13-14	5th order trefoil

important to realize that *no* thermal control of either M1 or M2 had yet been implemented, so the uncorrected wavefront aberration coefficients were sometimes several microns in magnitude.

The blue bars show the observed wavefront coefficients after correcting the mirror figure (as described in reference [8]). The coma and defocus were corrected by respectively tilting and pistoning the secondary mirror.

Below the bar graph are the image diffraction point spread functions corresponding to each set of aberrations. The starting image was a "blob" about 0.75-arcsec in diameter. After one correction, the psf is contained in a 0.1-arcsec box! The image however requires a second correction to become nearly diffraction limited. This is illustrated by the corrected measured wavefront shown in the blue bars. The remaining wavefront error generally grows with decreasing mode number. This is because higher-order correction creates spurious low-

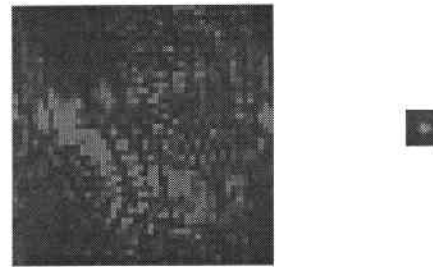
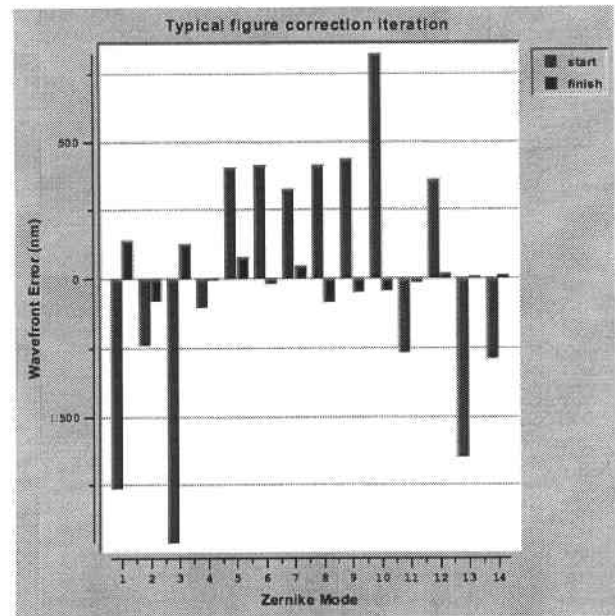


Figure 12: Top--Wavefront error (nm) is shown for 14 Zernike modes before (red) and after (blue) a single correction of primary mirror figure and secondary alignment. The initial aberrations are relatively large because neither M1 nor M2 were thermally controlled in mid 2000. Bottom--The calculated image psfs before (left, 0.75 x 0.75 arcsec box) and after (0.1 x 0.1 arcsec box) the correction. See text for more details.

order bending of the mirror. A second iteration generally removes the remaining errors.

The last figure in this section illustrates the effectiveness of correcting even a few low-order zernike modes by bending the primary mirror. The uncorrected *first-light* image of the binary sigma 2422 is shown with the image of the binary COU 453 after low-order figure and collimation corrections. In each case, there is no thermal control of either the primary or secondary borosilicate mirror.

VI. Software Design

The software is designed with a scripted GUI wrapping stand-alone C-routines. The compiled C gives the software computational speed while the GUI provides for flexible user control, data flow management, and graphical representation of the

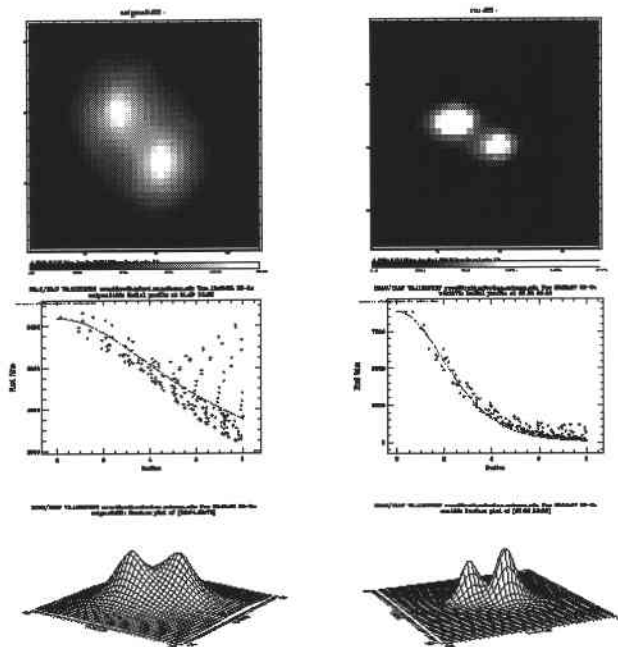


Figure 13: A comparison of binary images with and without low-order figure correction. There was no primary thermal control for either image. On the left is the first-light image of the binary sigma 2422 (sep $\sim 0.75''$) with no figure correction. On the right is an image of COU 453 (sep $\sim 0.6''$) after correcting for coma, astigmatism, defocus, trefoil, and 3rd-order spherical. Under each image is the IRAF radial energy distribution and surface plot. The IRAF gaussian fit to the radial energy profile gives a 0.35-arcsec FWHM to the corrected image of COU 453. This includes an obvious image elongation due to an elevation tracking error.

results. Since the core calculations are contained in the C-code, the analysis software can run independent of the GUI for control automation (e.g. closing the loop).

The solve mode can be changed to use wavefront gradients fitted only to Zernike polynomials (for either type of analyzer) or mode-independent phase reconstruction (currently for the interferometric device only). The latter is useful for identifying mirror figure errors that do not correspond to zernike polynomials (e.g. localized errors due to thermal or support control problems).

This section describes the software components. The GUI is written in TCL/TK and uses the Tix megawidget and BLT graphing extensions. Numerical Recipes routines written in C perform the calculations of section IV. The entire suite runs under Linux.

Data is exchanged between the GUI and C programs using either the TCL command pipeline or intermediate files. The GUI scripts collect parameters from the user which are passed to the C programs as command line arguments.

A. Main control window

Figure 14 shows the main toplevel window which controls the

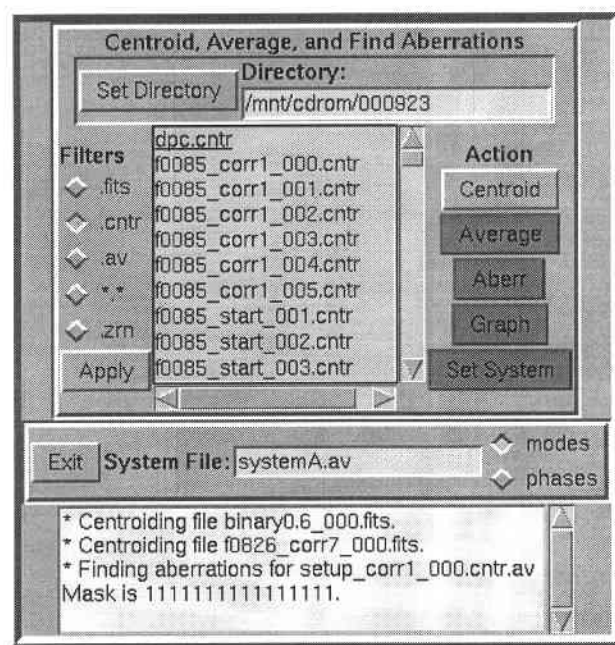


Figure 14: This window controls the data analysis from start to finish. Files are selected and batch-processed through the various action buttons. See text for details.

flow of data analysis from start to finish. The "Set Directory" button pops up a Tix megawidget for the selection of the data directory. FITS images are collected into this directory from the CCD using Elwood Downey's CAMERA program (also running in Linux).

The "Filters" radio buttons select the kind of file displayed in the scrolling listbox by using the file extension as a filter. Action buttons appropriate for this type of file are automatically turned green for the user. Listbox selections are made and then passed to C routines when the action button is depressed. The listbox supports multiple discontinuous selections and passes them to the action in batch mode. In this way, groups of files can be processed with a single click of the action button.

There is a scrolling text widget that reports the progress of the action buttons, command pipelines, and any errors that may be encountered.

B. Image Analysis

Before the wavefront aberrations can be calculated, the xy spot positions must be measured on the CCD. The centroid action provides highly accurate estimates of the gravitational center of the a given spot diagram, the centroids of all spots found, and the best-fit x and y magnifications of the grid.

The purpose of the "find centroids" code is to automate the process of obtaining information from the CCD image containing the interference spots. Prior to writing our own software, we tested the IRAF STARFIND routine, but found it required too much fine-tuning for different atmospheric conditions. It also tended to generate too many false positive spots unless the parameters were tweaked "just right".

The approach for our software is to: 1) remove camera artifacts such as hot pixels, low frequency image shading, and the "DC" pedestal signals present in the region of the interference spots, and 2) use the known geometry of the image to differentiate between the real spots and other artifacts while allowing for unknown global wavefront tilts from frame to frame.

An initial screening pass of the entire image is performed looking for bright spots whose area are too small to be actual $m=0$ interference and other camera artifacts. Since the spots we are trying to detect are narrow and high they would be composed strictly of high spatial frequencies. Fourier techniques (unsharp masking) were used to generate the high pass filtered image. The technique of unsharp masking consists of forming a low frequency image, and subtracting that from the original image containing low and high frequencies, leaving only the high frequency components.

An estimate of the image geometry was obtained from the low frequency image. A histogram of the pixel values was generated. Any regions of the image that contained pixels with values in the top one-half of the histogram were considered part of the pedestal that the spots resided on. First the center of gravity (CG) of the pedestal was determined as an estimate of the geometric center of the entire spot pattern (used for registering the global wavefront tilts between images). The outer radius of the pedestal was also computed and used to limit the area searched for spots.

The low frequency image was then subtracted from the original image producing an image of the spots with a gray level amplitude very near zero.

A loop was then started whose goal was to find all of the candidate $m=0$ spots and store their location in a list. This list was processed using the geometrical constraints (e.g. pixel spacing) to determine the spot positions. The loop executed as follows:

- 1) The brightest pixel remaining in the image was determined. To allow the algorithm to execute within acceptable time constraints an 8X8 "resolution pyramid" was employed reducing the search time by a factor of 64.

- 2) The coordinates of this pixel were used as the starting location of a region growing algorithm. The algorithm was allowed to search as long as it found pixels with grey scale values within a certain percentage of the peak value. We used

our estimated spot spacing to limit the size of the generated region.

- 3) The validity of the region was then checked by comparing the number of pixels found to the maximum allowed to determine if the spot has grown dangerously large.

- 4) Compare the region detected with those already found to prevent invalid overlapping spots.

- 5) If the spot passes all of the above tests, add it to the list of candidate spots.

- 6) Remove the current spot from the image by setting an area under the spot to zero.

- 7) Go to 1) and find the next brightest pixel.

Next we process our list of spot candidates as follows:

- 1) Determine a spot's CG using the original image data.

- 2) Search the entire list for its 8 nearest neighbors based on the spot's CG and our estimated spot spacing.

- 3) Sort the list so that the nearest neighbors are at the top of the list.

- 4) To refine our estimate of the spot spacing, we form a histogram of these 8 nearest neighbor distances. A rectangular window is used to scan the histogram. The width of the window is increased each pass until the sum of the spots under it is equal to half of the total (e.g. the 4 nearest each spot). The center of this window is used as our most likely estimate of interspot spacing.

- 5) The sorted list is scanned to determine if the 4 nearest neighbors are the proper distance and in the proper directions to be the left/right and above/below neighbors. Not all spots will have 4 close neighbors since some of them are located at the edge of the pattern.

- 6) Order the list so that the spots are increasing from left to right and top to bottom, omitting any that do not have acceptable neighbors.

This list with the associated Cgs is the final output.

C. Actions

Five action buttons are present in Figure 14:

- The Centroid button passes the selected FITS files to the "list centroids" routine described above.
- Groups of centroided files can be averaged together (e.g. to average seeing variations or increase signal to noise) with

the “Average” action.

- The “Aberr” action calculates the wavefront aberrations of centroided files by comparing them to a laser reference centroid file. “Set System” allows the selection of the laser reference centroid file used by the “Aberr” action. The type of solve used to calculate the wavefront errors is specified with two radio buttons. “Modes” uses a wavefront gradient solve, and “phases” uses a raw phase reconstruction (equations 2 or 7 respectively). Both are described in Section IV above.
- “Graph” allows the graphical display of centroided files (described below). A BLT graph widget provides the user a way to interact with the centroid files (Figure 15). The

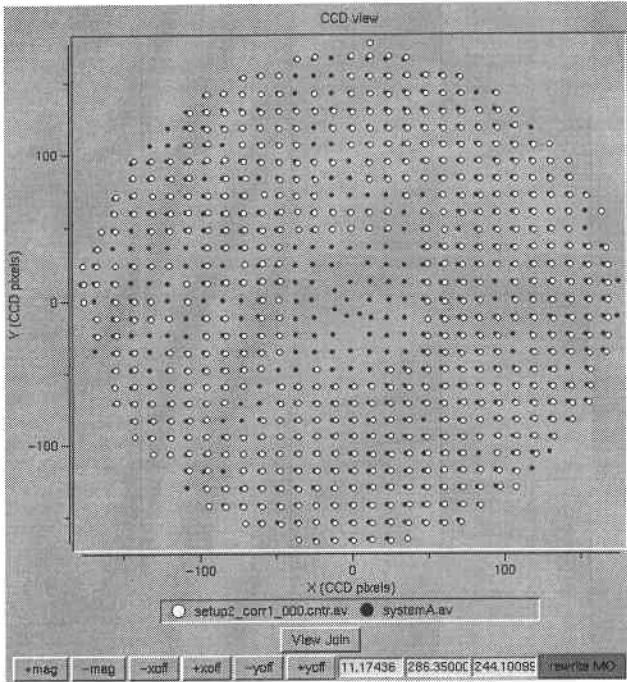


Figure 15: Interactive graphing widget for viewing and manipulating centroid files. Here the reference (solid red) and stellar spot diagrams are shown (intentionally displaced for clarity). The graph supports dynamic zooming for closer inspections. The user may manually fine-tune the registration of the spots if the automatic registration is insufficiently accurate.

widget supports dynamic zooming for closer inspections of groups of spots. Sometimes, it’s useful to simply plot a centroid file to see how many spots were found in the image. It’s also useful to plot the stellar spot diagrams against the laser reference spots in order to verify proper registration prior to calculating the wavefront aberrations. Missing spots do not pose a problem because the calculations automatically adapt themselves to find solutions using whatever spots are available.

Once the two centroid files are plotted, the “View Join” button applies the estimated registration and differential magnification to shows how well the computer automatically registered the frames.

The centroid files must be registered to less than half the spacing between individual spots (typically ~10 pixels) so that the

computer can properly identify corresponding spots. Sometimes very large low order aberrations preclude an accurate automatic registration. Buttons along the bottom of the graphing widget allow the user to tweek the registration by manually translating and magnifying one of the centroid files. Using the “Rewrite MO” button, the new magnifications and offsets overwrite the original ones. These parameters are used only for registration purposes so that the computer can generate linked lists of corresponding spots. The wavefront aberrations are calculated using the original unaltered centroids from the FITS image.

D. Wavefront display windows

After the “Aberr” action calculates the wavefront polynomial coefficients, they can be loaded into another toplevel window for display as shown in Figure 16. A checkbox allows each mode to be individually turned on or off for the calculation of primary mirror correction forces, pupil and image displays (described below).

The lower two entry boxes and the “Add to Log” action allow the user to maintain the zernike coefficients in a log file with comments for each entry. If a new log file name is chosen, the first entry is preceded by labels identifying the columns of coefficients. If the log file name already exists, new data and comments are appended to the file.

The window for image display of results is shown in Figure 17. After the user selects which Zernike modes to analyze (checkboxes in Figure 16), the “Pupil modes” action sends greyscale maps of the pupil aberrations and image diffraction psf to this window. Three entry fields allow the image of the psf to be changed. The “+/- Det” field shifts the image plane of the diffraction calculation away from the nominal focal plane (specified in microns). “Field” specifies the box size in arcseconds for scaling the image. “Range %” allows the user to specify the fraction of image intensity to display. For example, 100% maps the entire image intensity to the display while 25% maps the lowest 25% of intensity to the image. This function allows the faint structure of the psf to be viewed. Once any of these fields are updated, the “Pupil modes” action must be clicked to update the display.

The diffraction image is constructed by dividing the pupil wavefront into a coarse grid. The phase from each grid point is summed into each pixel of a virtual detector using the optical geometry of the telescope. The current coarse sampling produces image aliases at spacings of about 1.5 arc second (at a visible wavelengths). In order to avoid confusion for poor images, the pupil sampling would need to be increased at the expense of speed.

In addition, the rms wavefront phase errors are calculated and displayed in a color-coded BLT barchart widget. The right most bar shows the rms error of all the checkbox-selected

VII. Summary

The theory, development and implementation of an interferometric Hartmann wavefront analyzer for the 6.5m MMT is briefly described. In practice, we found the interferometric technique worked very well. It has sufficient dynamic range to measure wavefront aberration coefficients as large as several microns, yet consistently and repeatably detects small wavefront errors in the 10nm range. Software was developed to interact with the instrument and to control mirror figure and collimation corrections. We found that 2 correction iterations produce image psfs near 0.1-arcsec even when starting with very large errors.

The major limitation seems to be poor interferometric spot visibility when the atmospheric seeing is greater than about 1.5 arcsec. Although mirror figure correction is relatively unimportant under these conditions, it is very difficult to measure the wavefront at all. Therefore correcting simple collimation and focus is difficult under circumstances where the observer would surely continue using the telescope. In the presence of poor seeing, longer integration times did not substantially improve spot visibility. One solution is to measure at short integration times (where the spots are distinct) and average a large number of spot positions in order to remove seeing effects. Tapio Korhonen has since shown that this limitation is a consequence of our Hartmann mask geometry. Doubling the number of apertures along x and y would have doubled our tolerance to seeing --resulting in the technique working in the presence of 3-arcsec seeing.

Although we proved that we can adequately correct mirror figure and collimation, there remains much to be done. Better quantification of the results of mirror bending especially for higher order modes is needed. The effectiveness of bending Zernike modes vs. using the natural mirror modes needs investigation. An analysis of localized figure errors is yet to be done so that for example, we can look for isolated errors such as bumps over the hardpoint connections. Finally the construction of the lower resolution wavefront sensors for routine nightly use with automated active "closing of the loop" needs to be accomplished.

VIII. Acknowledgements

We thank the MMTO mountain operations staff, especially Dennis Smith, Mike Alegria, and Bill Kindred for instrument support. We appreciate the MMT telescope operators (Carol Heller, John McAfee, and Ale Milone) for their help and enthusiasm during the telescope checkout period. Tom Trebisky helped the software through a few rough spots. We thank the MMTO director, Craig Foltz, for authorizing funds and manpower in this experimental direction. Tapio Korhonen generously answered many questions about using and implementing an interferometric Hartmann wavefront analyzer.

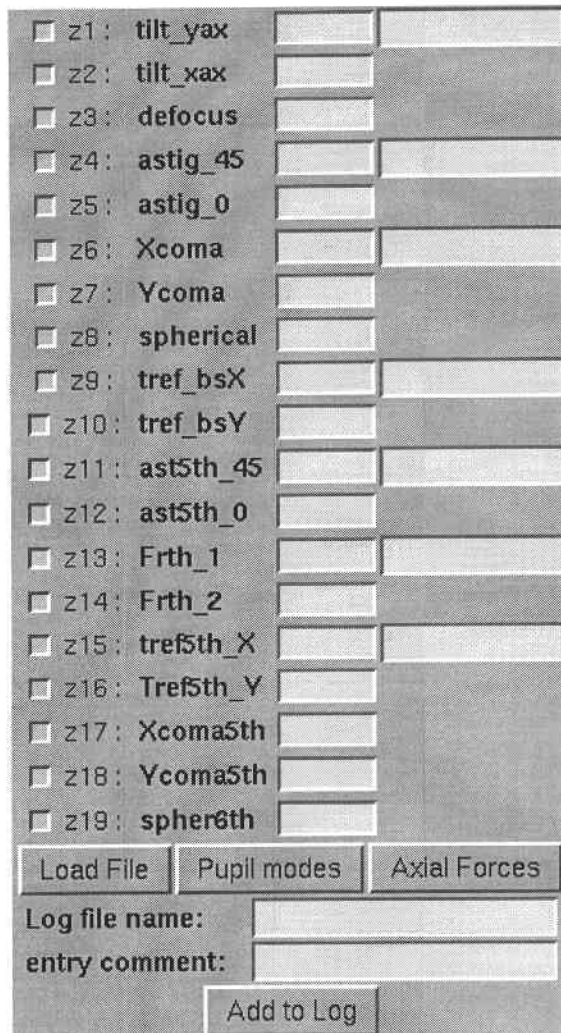


Figure 16: Window for the display of Zernike coefficients fitted to the wavefront errors. Each mode coefficient (nm) is displayed. Total mode strength and angle are shown in the rightmost boxes. Checkbuttons allow individual modes to be selected for calculations of axial support forces and/or diffraction image psfs. The lower area is for maintaining the results in a log file.

modes combined. Like the graphing widget previously described, the barchart supports dynamic zooming.

The "Axial Force" action of Figure 16 calculates the primary mirror axial force distribution that corrects the aberrations selected with the checkbuttons. A greyscale map, showing the distribution of axial forces is sent to the display window. In addition, a Tix scrolling list megawidget allows the user to easily inspect the correction forces before applying them to the primary mirror support system.

The c-programs construct XPM images from the results of the calculations and save them to files with standard names. The TCL/TK scripts read the files and display them using the XPM image support provided by the Tix extension.

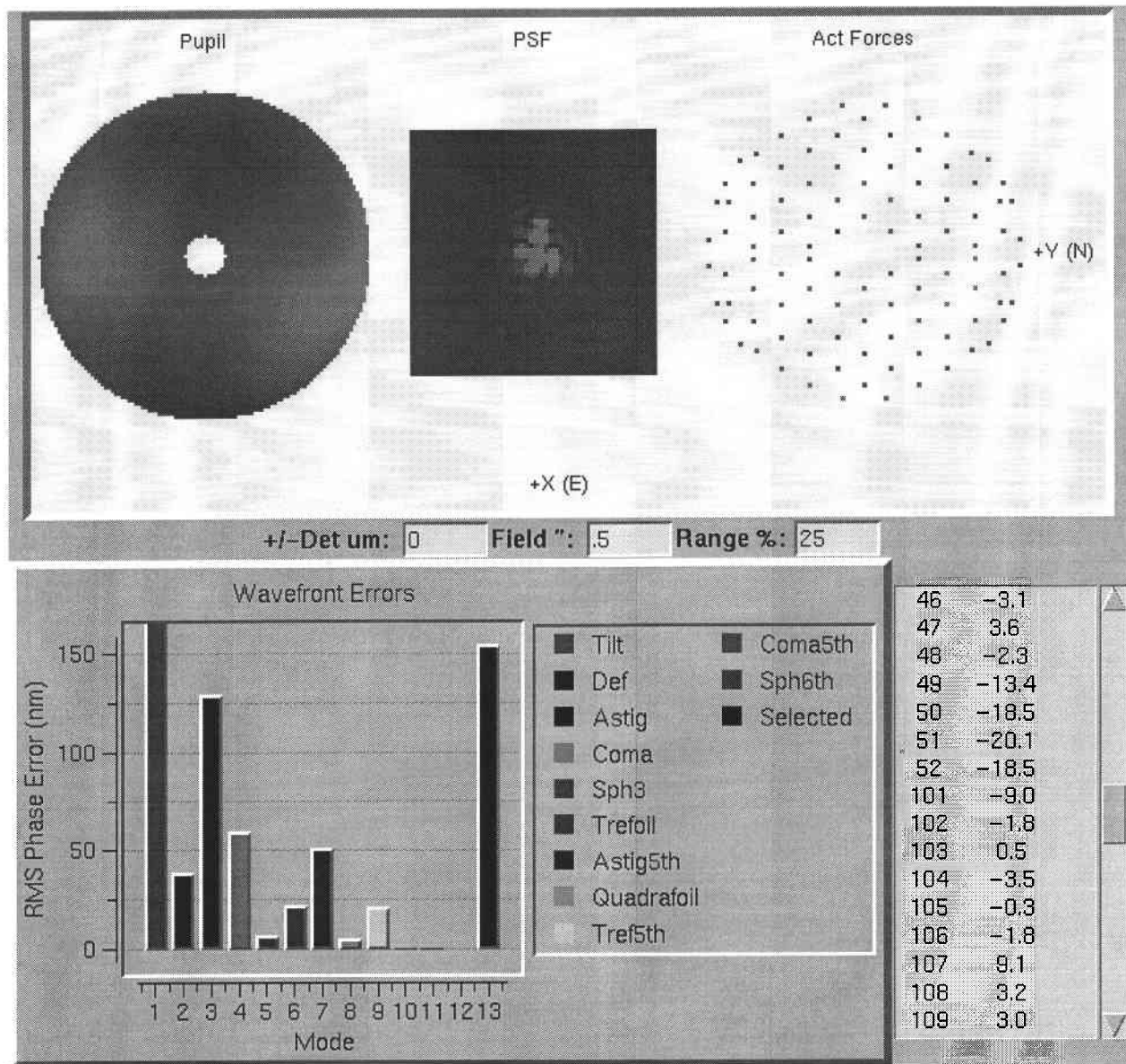


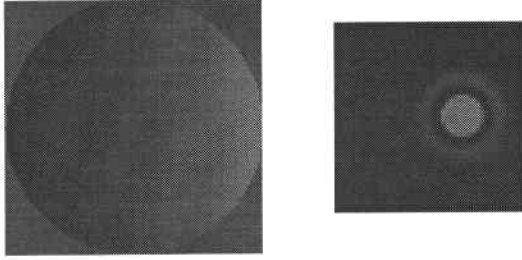
Figure 17: Results display window. Images of the pupil aberrations, diffraction image, and axial force corrections are shown for the user-selected Zernike coefficients of the solution. Three entry fields allow the user to modify the psf by adjusting detector position, field size, and intensity range of the image. A bar chart shows the rms wavefront phase errors due to the individual modes. A color map of the actuator forces is shown along with a scrolling list allowing the user to inspect the correction forces before sending them to the primary mirror support system.

IX. Appendix A: Wavefront Expansion

Currently, the wavefront error is fit to 19 Zernike polynomials. Each polynomial is presented in polar and monomial forms along with the monomial gradients. In addition, the pupil phase and image psf for the modes is shown. The diffraction psfs were calculated with the instrument software described above. We adopt one of the standard coordinate conventions

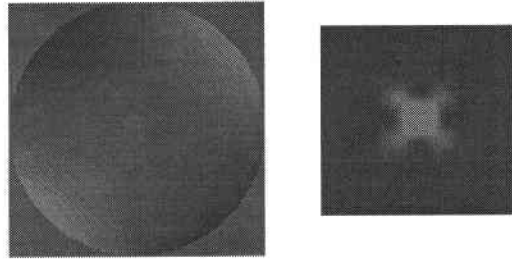
for Zernike polynomials that has $\theta = 0$ along the y-axis increasing toward the x-axis. The diagrams have +y up and +x to the right. Each psf is illustrated in a sub-arcsec square box with a coefficient of a few hundred nanometers in that particular mode. Typically, the image is scaled to show the lowest 25% of intensity.

A. Z1: Tilt about y-axis:



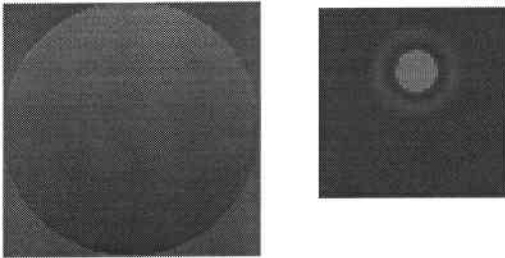
$$\begin{aligned}\rho \sin(\theta) &= x \\ \frac{\partial}{\partial x} &= 1 \\ \frac{\partial}{\partial y} &= 0\end{aligned}$$

D. Z4: Astigmatism +/-45 deg:



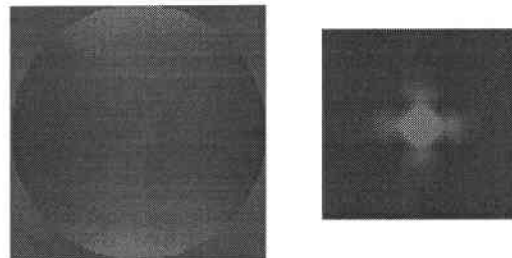
$$\begin{aligned}\rho^2 \sin(2\theta) &= 2xy \\ \frac{\partial}{\partial x} &= 2y \\ \frac{\partial}{\partial y} &= 2x\end{aligned}$$

B. Z2: Tilt about x-axis:



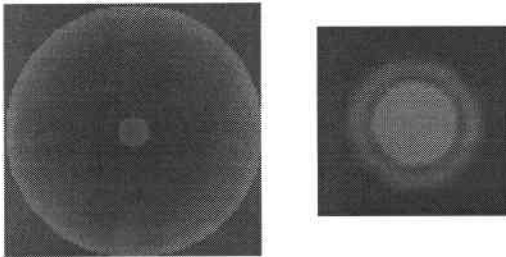
$$\begin{aligned}\rho \cos(\theta) &= y \\ \frac{\partial}{\partial x} &= 0 \\ \frac{\partial}{\partial y} &= 1\end{aligned}$$

E. Z5: Astigmatism 0,90 deg:



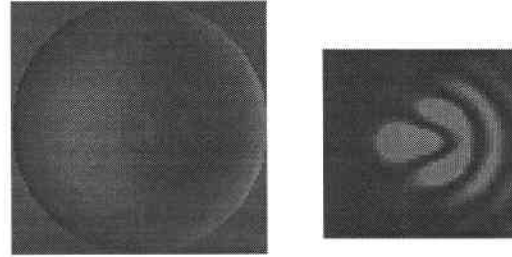
$$\begin{aligned}\rho^2 \cos(2\theta) &= y^2 - x^2 \\ \frac{\partial}{\partial x} &= -2x \\ \frac{\partial}{\partial y} &= 2y\end{aligned}$$

C. Z3: Defocus:



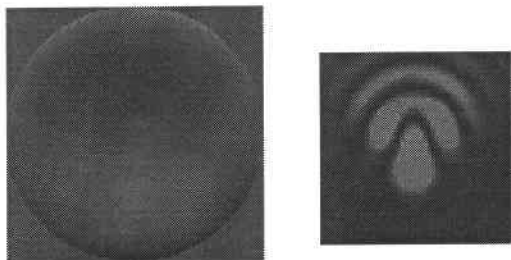
$$\begin{aligned}2\rho^2 - 1 &= 2x^2 + 2y^2 - 1 \\ \frac{\partial}{\partial x} &= 4x \\ \frac{\partial}{\partial y} &= 4y\end{aligned}$$

F. Z6: Coma along x:



$$\begin{aligned}(3\rho^2 - 2\rho)\sin(\theta) &= 3x^3 + 3xy^2 - 2x \\ \frac{\partial}{\partial x} &= 9x^2 + 3y^2 - 2 \\ \frac{\partial}{\partial y} &= 6xy\end{aligned}$$

G. Z7: Coma along y:

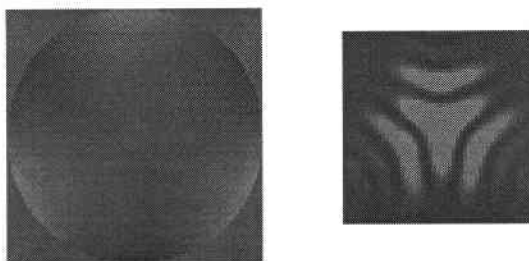


$$(3\rho^2 - 2\rho)\cos(\theta) = 3y^3 + 3yx^2 - 2y$$

$$\frac{\partial}{\partial x} = 6xy$$

$$\frac{\partial}{\partial y} = 3x^2 + 9y^2 - 2$$

J. Z10: Trefoil -- base on y-axis

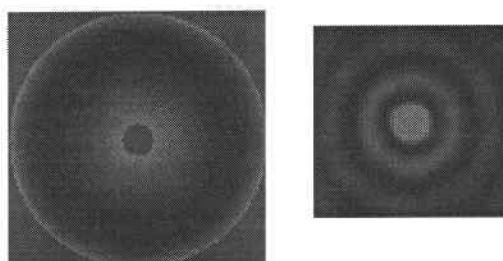


$$\rho^3 \cos(3\theta) = y^3 - 3x^2y$$

$$\frac{\partial}{\partial x} = -6xy$$

$$\frac{\partial}{\partial y} = 3y^2 - 3x^2$$

H. Z8: 3rd order Spherical:

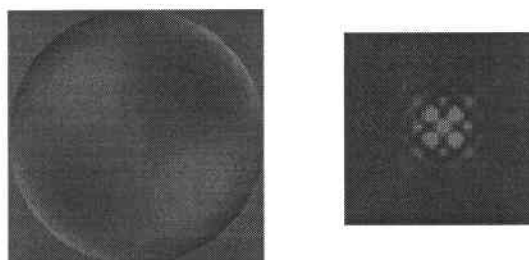


$$6\rho^4 - 6\rho^2 + 1 = 6x^4 + 6y^4 + 12x^2y^2 - 6x^2 - 6y^2 + 1$$

$$\frac{\partial}{\partial x} = 24x^3 + 24xy^2 - 12x$$

$$\frac{\partial}{\partial y} = 24y^3 + 24x^2y - 12y$$

K. Z11: 5th-order astigmatism -- +/- 45 deg

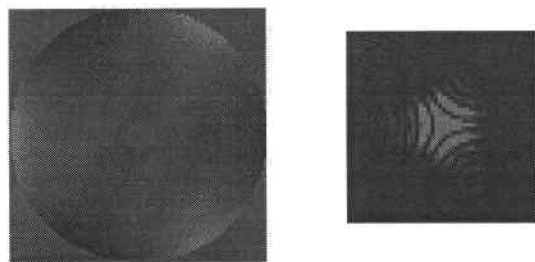


$$(4\rho^4 - 3\rho^2)\sin(2\theta) = 8x^3y + 8y^3x - 6xy$$

$$\frac{\partial}{\partial x} = 8y^3 + 24x^2y - 6y$$

$$\frac{\partial}{\partial y} = 8x^3 + 24y^2x - 6x$$

I. Z9: Trefoil -- base on x-axis

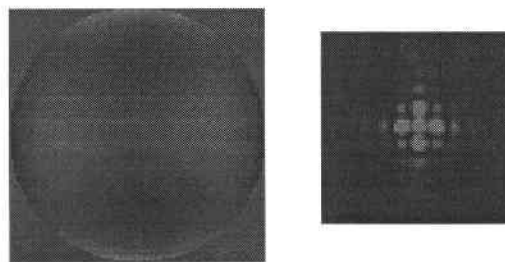


$$\rho^3 \sin(3\theta) = 3xy^2 - x^3$$

$$\frac{\partial}{\partial x} = 3y^2 - 3x^2$$

$$\frac{\partial}{\partial y} = 6xy$$

L. Z12: 5th-order astigmatism -- 0,90 deg

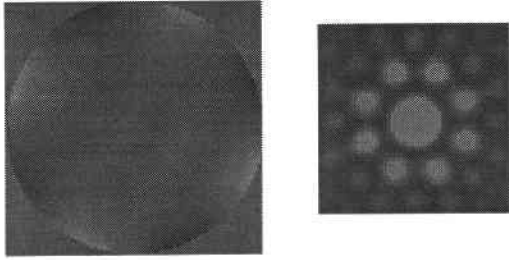


$$(4\rho^4 - 3\rho^2)\cos(2\theta) = 4y^4 - 4x^4 + 3x^2 - 3y^2$$

$$\frac{\partial}{\partial x} = 6x - 16x^3$$

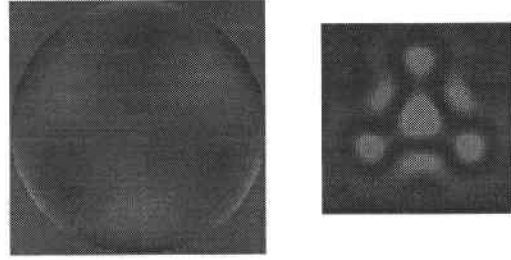
$$\frac{\partial}{\partial y} = 16y^3 - 6y$$

M. Z13: Quatrefoil 1



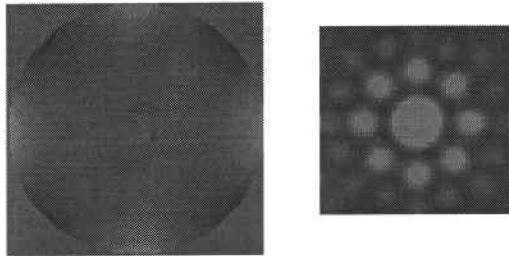
$$\begin{aligned} \rho^4 \sin(4\theta) &= 4y^3x - 4x^3y \\ \frac{\partial}{\partial x} &= 4y^3 - 12x^2y \\ \frac{\partial}{\partial y} &= 12y^2x - 4x^3 \end{aligned}$$

P. Z16: 5th-order Trefoil -- base on y-axis



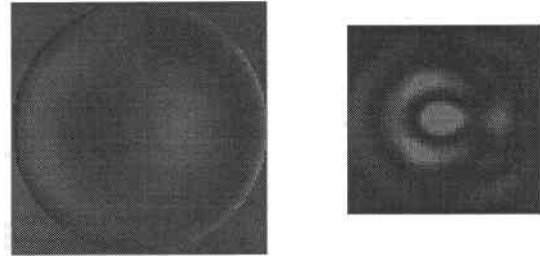
$$\begin{aligned} (5\rho^5 - 4\rho^3)\cos(3\theta) &= 5y^5 - 15x^4y - 10x^2y^3 + 12x^2y - 4y^3 \\ \frac{\partial}{\partial x} &= 24xy - 20xy^3 - 60x^3y \\ \frac{\partial}{\partial y} &= 12x^2 - 12y^2 + 25y^4 - 30x^2y^2 - 15x^4 \end{aligned}$$

N. Z14: Quatrefoil 2



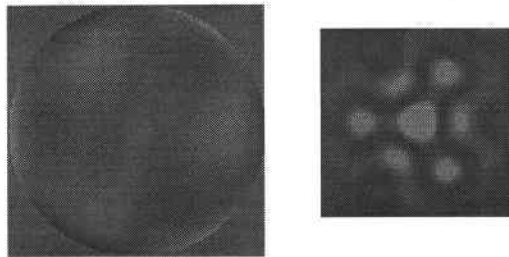
$$\begin{aligned} \rho^4 \cos(4\theta) &= y^4 - 6x^2y^2 + x^4 \\ \frac{\partial}{\partial x} &= 4x^3 - 12xy^2 \\ \frac{\partial}{\partial y} &= 4y^3 - 12x^2y \end{aligned}$$

Q. Z17: 5th-order Coma along x-axis



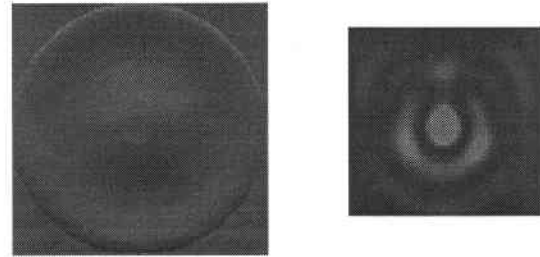
$$\begin{aligned} (10\rho^5 - 12\rho^3 + 3\rho)\sin(\theta) &= 10x^5 + 20x^3y^2 + 10xy^4 - 12x^3 - 12xy^2 + 3x \\ \frac{\partial}{\partial x} &= 50x^4 + 60x^2y^2 + 10y^4 - 36x^2 - 12y^2 + 3 \\ \frac{\partial}{\partial y} &= 40x^3y + 40xy^3 - 24xy \end{aligned}$$

O. Z15: 5th-order Trefoil -- base on x-axis



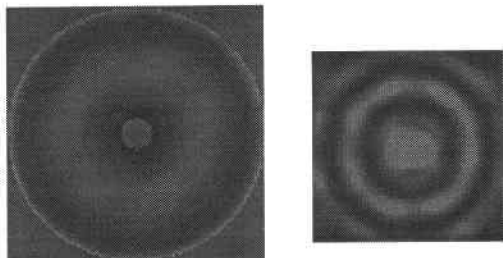
$$\begin{aligned} (5\rho^5 - 4\rho^3)\sin(3\theta) &= 15xy^4 - 5x^5 + 10x^3y^2 + 4x^3 - 12xy^2 \\ \frac{\partial}{\partial x} &= 15y^4 - 25x^4 + 30x^2y^2 + 12x^2 - 12y^2 \\ \frac{\partial}{\partial y} &= 60xy^3 + 20x^3y - 24xy \end{aligned}$$

R. Z18: 5th-order Coma along y-axis



$$\begin{aligned} (10\rho^5 - 12\rho^3 + 3\rho)\cos(\theta) &= 10y^5 + 10yx^4 + 20x^2y^3 - 12yx^2 - 12y^3 + 3y \\ \frac{\partial}{\partial x} &= 40yx^3 + 40xy^3 - 24xy \\ \frac{\partial}{\partial y} &= 10x^4 + 60x^2y^2 + 50y^4 - 12x^2 - 36y^2 + 3 \end{aligned}$$

S. Z19: 6th-order Spherical



$$20\rho^6 - 30\rho^4 + 12\rho^2 - 1 =$$

$$20x^6 + 60x^4y^2 + 60x^2y^4 + 20y^6 - 30x^4 - 60x^2y^2 - 30y^4 + 12x^2 + 12y^2 - 1$$

$$\frac{\partial}{\partial x} = 120x^5 + 240x^3y^2 + 120xy^4 - 120x^3 - 120xy^2 + 24x$$

$$\frac{\partial}{\partial y} = 120x^4y + 240x^2y^3 + 120y^5 - 120x^2y - 120y^3 + 24y$$

X. Appendix B: Software components

This section provides a brief description of all the software components.

A. script

- ihwfs.tcl: TCL/TK script that provides the GUI wrapper for all the C-programs. The script dynamically loads the extensions Tix and BLT using the "package require" command.

B. Numerical recipes

Four numerical recipes routines are used:

- nrutil.c for matrix and vector definitions and memory management.
- pythag.c
- svdcmp.c for singular value decomposition of matrices that need to be inverted.
- svbksb.c to backsolve the SVD matrix for the unknown quantities.

C. C library support

Several libraries were written to provide general utilities for the core C analysis programs.

- fileio.c, .h provides support for moving vectors and matrices to/from disk files and memory. It also contains a routine for reading the magnifications and offsets from centroided files.
- WFSlib.c, .h provides wavefront manipulation support. There are routines that create the wavefront gradient and phase reconstruction matrices. Pupil sampling routines solve for the rms phase errors and return vectors of resampled of Zernike polynomials. Another routine takes two

centroid files and produces a linked list of spots created by the same phase apertures (or lenslets).

- wfs_image.c makes an XPM image out of a 2D array.
- zernike.c, .h organize the zernike polynomials and their xy partial derivatives.
- optics.h is a symbolic link to a file which stores the optical parameters and physical dimensions of the telescope. Also stored are the Hartmann or lenslet mask geometries and their projections onto the entrance aperture as well as the scaling of spot motion to wavefront errors. Currently, there are two files: mmtf9_hires.h for the interferometric Hartmann wavefront analyzer with high resolution Hartmann mask on the f/9 MMT Cass focus and vattopticsORG.h for the prototype interferometric device on the VATT telescope.

D. Analysis C programs

- list_centroids.c takes FITS images as input and returns the centroid positions of all spots, the apparent x and y magnifications of the spot spacings, and an estimate of the gravitational center of the interferogram to be used for registering multiple frames.
- getZernikesAndPhases.c calculates the Zernike coefficients that fit observed wavefront errors. Depending on a command line flag, it either fits discrete wavefront slopes to the differentiated Zernike monomials (Shack Hartmann mode) or does a raw phase reconstruction to discrete phase differences formed by aperture quartets (Interferometric mode).
- pup_psf.c generates pupil phase and diffraction images from the gradient wavefront solution.
- pup_discretePhs.c generates a discrete pupil phase map and diffraction image from the phase reconstruction solution.
- bcv.c converts wavefront errors to primary mirror axial force corrections using the BCV Italia influence functions.
- ihaverage.c takes a stack of centroid files and averages the xy spot displacements.
- Makefile for upkeep of the whole mess. To re-compile the core routines, type "make -W optics.h newoptics".

XI. References

- [1] T. K. Korhonen, "Interferometric Method for Optical Testing and Wavefront Error Sensing," *SPIE* **444**, 249-252 (1984).
- [2] T. K. Korhonen, S. T. Haarala, J. O. Piironen, and A. K. Sillanpaa, "Interferometric Optical Test and Diffraction Based Image Analysis," *SPIE* **628**, p. 486-491 (1986).
- [3] T. Korhonen, T. Lappalainen, and A. Sillanpaa, "Hartmann Interferometric Testing of Large Mirrors," *SPIE* **1531**, p. 44-49 (1991).
- [4] R. N. Wilson, *Reflecting Telescope Optics II*, Section 2.3.3.3 "Interferometric modification of the Hartmann test," pp. 158-161, Springer.

- [5] S.C West, R. H Nagel, D. Harvey, A. Brar, B. Phillips, J. Ray, T.J. Trebisky, R. Cromwell, N.J. Woolf, C. Corbally, R. Boyle, D. Blanco, and L. Otten, "Progress at the Vatican Advanced Technology Telescope," *Optical Telescopes of Today and Tomorrow*, Proc. SPIE **2871**, p. 74, ed. Arne Arnenberg, Hven Sweden. (<http://nemo.as.arizona.edu/~swest/pdfs/vattspie.pdf>)
- [6] S. C. West, D. Fisher, and M. Nelson, "VATT optical performance during 98 Oct as measured with an interferometric hartmann wavefront sensor," *MMTO Internal Technical Memo #00-01*, Oct. 2000. (<http://nemo.as.arizona.edu/~swest/pdfs/vattwfs1998.pdf>)
- [7] B. R. Hunt, "Matrix formulation of the reconstruction of phase values from phase differences," *J. Opt. Soc. Am* **69** #3, (1979).
- [8] S. C. West and H. M. Martin, "Correcting 6.5m Primary Mirror Figure Errors with the Active Supports," *MMTO Conversion Technical Memo #00-2*, 18 Jan 2000. (<http://nemo.as.arizona.edu/~swest/pdfs/figureCorrectionsMemo.pdf>)
- [9] H.M. Martin, S.P. Callahan, B. Cuerden, W.B. Davison, S.T. DeRigne, L.R. Dettmann, G. Parodi, T.J. Trebisky, S.C. West, and J.T. Williams, "Active Supports and Force Optimization for the MMT Primary Mirror," *Advanced Technology Optical Telescopes VI*, L.M. Stepp ed., SPIE **3352**, 513 (1998).